Supporting Information

Atomistic Origin of Lattice Softness and Its Impact on Structural and Carrier Dynamics in Perovskites

*Zhendong Guo, Jing Wang, Prof. Wan-Jian Yin**
College of Energy, Soochow Institute for Energy and Materials Innovations (SIEMIS), Soochow University, Suzhou 215006, China

Jiangsu Provincial Key Laboratory for Advanced Carbon Materials and Wearable Energy Technologies, Soochow University, Suzhou 215006, China

Key Lab of Advanced Optical Manufacturing Technologies of Jiangsu Province & Key Lab of Modern Optical Technologies of Education Ministry of China, Soochow University, Suzhou 215006, China
Email: wjyin@suda.edu.cn

Bulk modulus of halide and chalcogenide perovskites

Theoretical Formulation of bulk modulus for perovskites ABX_3: In our phenomenological model, the total energy (E) of perovskites ABX_3 per unit cell (cf. Eq, (1)) is divided into two parts: the attraction and repulsion contributions, which are described by the Madelung energy as $U_{Mad} = \frac{\alpha \cdot q_B \cdot q_X}{d}$ and the repulsion term of Lennard-Jones potentials as $U_{rep} = \frac{\beta}{d^n}$, respectively. Here, α and β are constants, and $q_B(q_X)$ and d represent the ionic charge and B-X bond length, respectively.

$$E = \frac{\alpha \cdot q_B \cdot q_X}{d} + \frac{\beta}{d^n} \tag{1}$$

At the equilibrium status with $d = d_{B-X}$, we can obtain:

$$\left.\frac{\partial E}{\partial d}\right|_{d=d_{B-X}} = -\alpha \cdot q_B \cdot q_X \cdot d_{B-X}^{-2} - n \cdot \beta \cdot d_{B-X}^{-(n+1)} = 0 \tag{2}$$

where d_{B-X} represents the equilibrium B-X bond length. By reformulating Eq. (2), we achieve:

$$d_{B-X}^{-(n-1)} = -\frac{\alpha \cdot q_B \cdot q_X}{n \cdot \beta} \tag{3}$$

Take the cubic phase perovskites as an example. The volume per unit-cell (Ω) can be simply given by:

$$\Omega = (2d)^3 \tag{4}$$

Therefore, we achieve:

$$d = \frac{1}{2} \cdot \Omega^{\frac{1}{3}} \tag{5}$$

By combining Eq. (1) and (5), we can obtain the expression of E as a function of Ω:

$$E = 2\alpha \cdot q_B \cdot q_X \cdot \Omega^{-\frac{1}{3}} + 2^n \cdot \beta \cdot \Omega^{-\frac{n}{3}} \tag{6}$$

According to the definition of bulk modulus (B_{mod}) of solids, we attain:

$$B_{mod} = \Omega \cdot \left.\frac{\partial^2 E}{\partial d^2}\right|_{d=d_{B-X}} = \frac{8}{9}\alpha \cdot q_B \cdot q_X \cdot \Omega^{-\frac{4}{3}} + 2^n \cdot \frac{n(n+3)}{9} \cdot \beta \cdot \Omega^{-\frac{n+3}{3}}$$

$$= \frac{1}{18}\alpha \cdot q_B \cdot q_X \cdot d_{B-X}^{-4} + \frac{n(n+3)}{72} \cdot \beta \cdot d_{B-X}^{-(n+3)} \tag{7}$$

By combining Eq. (3) and (7), we finally obtain:

$$B_{mod} = -\frac{n-1}{72} \cdot \alpha \cdot q_B \cdot q_X \cdot d_{B-X}^{-4} \tag{8}$$

Table S1. Calculated bulk moduli (GPa) of studied halide and chalcogenide perovskites in the cubic (B_c) and tetragonal (B_t) phases.

	$KCaCl_3$	$KCaBr_3$	$KCaI_3$	$KSrCl_3$	$KSrBr_3$	$KSrI_3$	$KBaCl_3$	$KBaBr_3$	$KBaI_3$
B_c	25.325	21.121	16.227	21.639	18.223	14.308	17.910	15.247	12.404
B_t	24.661	20.645	16.594	21.440	18.290	14.678	17.604	15.437	13.133
	$KGeCl_3$	$KGeBr_3$	$KGeI_3$	$KSnCl_3$	$KSnBr_3$	$KSnI_3$	$KPbCl_3$	$KPbBr_3$	$KPbI_3$
B_c	26.315	22.164	17.587	21.358	18.374	14.725	20.190	17.198	13.989
B_t	25.607	21.921	17.945	21.049	18.095	15.297	19.617	17.049	14.385
	$RbCaCl_3$	$RbCaBr_3$	$RbCaI_3$	$RbSrCl_3$	$RbSrBr_3$	$RbSrI_3$	$RbBaCl_3$	$RbBaBr_3$	$RbBaI_3$
B_c	24.955	20.865	16.104	21.413	18.014	14.229	17.759	15.208	12.362
B_t	24.205	20.481	16.130	20.664	17.662	14.007	17.233	14.904	12.965
	$RbGeCl_3$	$RbGeBr_3$	$RbGeI_3$	$RbSnCl_3$	$RbSnBr_3$	$RbSnI_3$	$RbPbCl_3$	$RbPbBr_3$	$RbPbI_3$
B_c	26.094	21.854	17.327	21.174	18.233	14.635	20.045	17.072	13.900
B_t	25.456	21.482	17.422	20.696	17.743	14.857	19.529	16.765	13.978
	$CsCaCl_3$	$CsCaBr_3$	$CsCaI_3$	$CsSrCl_3$	$CsSrBr_3$	$CsSrI_3$	$CsBaCl_3$	$CsBaBr_3$	$CsBaI_3$
B_c	24.417	20.427	15.924	21.066	17.658	14.145	17.602	15.060	12.310
B_t	23.508	20.048	15.794	20.159	16.936	13.737	16.889	14.429	12.815
	$CsGeCl_3$	$CsGeBr_3$	$CsGeI_3$	$CsSnCl_3$	$CsSnBr_3$	$CsSnI_3$	$CsPbCl_3$	$CsPbBr_3$	$CsPbI_3$
B_c	25.372	21.282	17.049	20.905	18.059	14.459	19.802	16.887	13.807
B_t	25.302	21.096	16.894	20.412	17.643	14.317	19.299	16.588	13.552
	$CaTiO_3$	$CaTiS_3$	$CaTiSe_3$	$CaZrO_3$	$CaZrS_3$	$CaZrSe_3$	$CaHfO_3$	$CaHfS_3$	$CaHfSe_3$
B_c	175.596	78.517	64.849	154.922	74.498	61.601	166.275	75.997	62.986
B_t	170.635	76.569	63.119	150.444	72.423	60.235	162.642	73.514	61.103
	$CaSiO_3$	$CaSiS_3$	$CaSiSe_3$	$CaGeO_3$	$CaGeS_3$	$CaGeSe_3$	$CaSnO_3$	$CaSnS_3$	$CaSnSe_3$
B_c	216.200	73.881	56.924	170.545	62.434	50.139	149.462	56.743	46.828
B_t	218.594	75.825	59.110	170.157	65.652	48.989	145.868	60.801	44.327
	$SrTiO_3$	$SrTiS_3$	$SrTiSe_3$	$SrZrO_3$	$SrZrS_3$	$SrZrSe_3$	$SrHfO_3$	$SrHfS_3$	$SrHfSe_3$
B_c	170.192	77.058	64.491	151.846	73.292	60.796	162.770	74.922	62.073
B_t	166.012	74.141	62.510	148.611	70.252	59.113	159.616	72.405	60.713
	$SrSiO_3$	$SrSiS_3$	$SrSiSe_3$	$SrGeO_3$	$SrGeS_3$	$SrGeSe_3$	$SrSnO_3$	$SrSnS_3$	$SrSnSe_3$
B_c	201.487	70.101	55.055	158.199	60.449	49.419	140.614	55.951	46.008
B_t	202.926	72.528	57.365	157.520	62.454	47.375	135.865	57.628	43.393
	$BaTiO_3$	$BaTiS_3$	$BaTiSe_3$	$BaZrO_3$	$BaZrS_3$	$BaZrSe_3$	$BaHfO_3$	$BaHfS_3$	$BaHfSe_3$
B_c	161.939	76.469	63.177	149.259	71.794	59.805	154.091	73.562	61.054
B_t	160.796	73.653	61.101	148.402	68.409	57.920	153.862	71.202	59.060
	$BaSiO_3$	$BaSiS_3$	$BaSiSe_3$	$BaGeO_3$	$BaGeS_3$	$BaGeSe_3$	$BaSnO_3$	$BaSnS_3$	$BaSnSe_3$
B_c	177.717	67.071	51.869	137.695	59.220	47.210	131.659	55.500	45.094
B_t	179.850	69.491	52.929	137.021	60.126	45.701	127.359	56.890	42.395

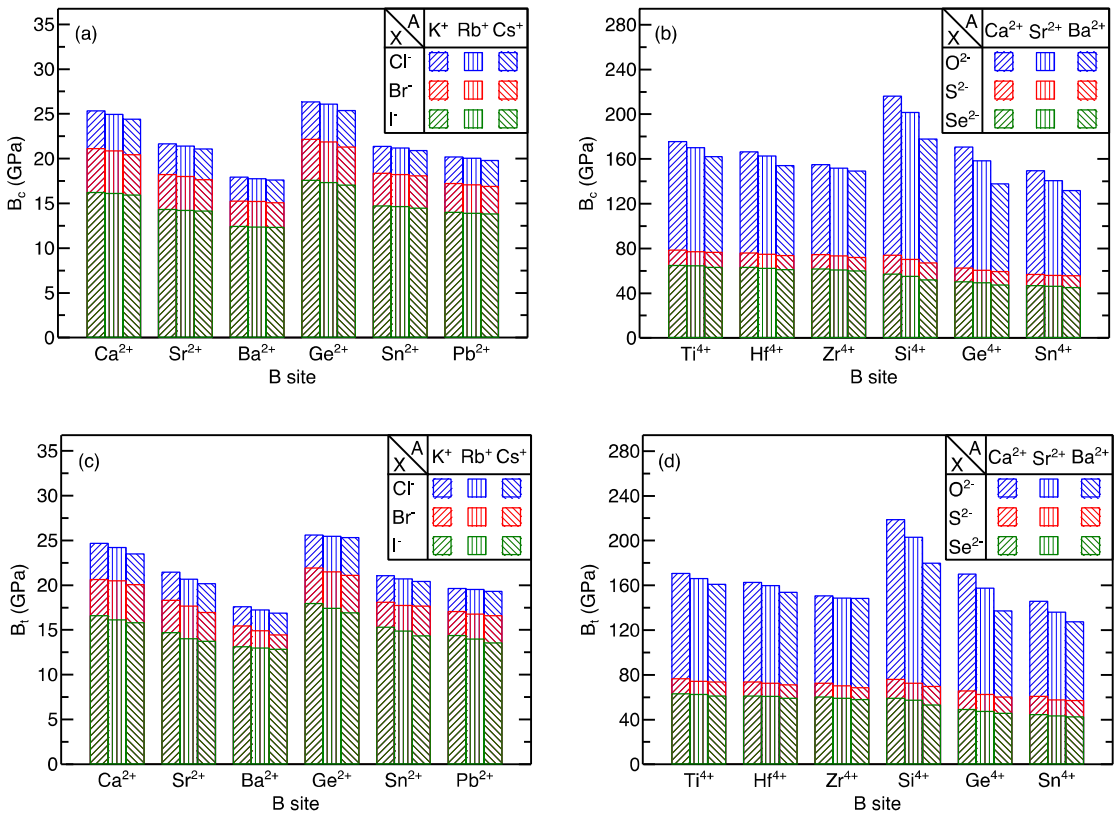

Figure S1. Calculated bulk moduli of 54 halide and 54 chalcogenide perovskites ABX_3 in their cubic (a, b) and tetragonal (c, d) phases as a function of composition ions. For the sake of comparison, the B-site cations belonging to the same groups in the periodic table of elements are arranged in the order of the radius increasing.

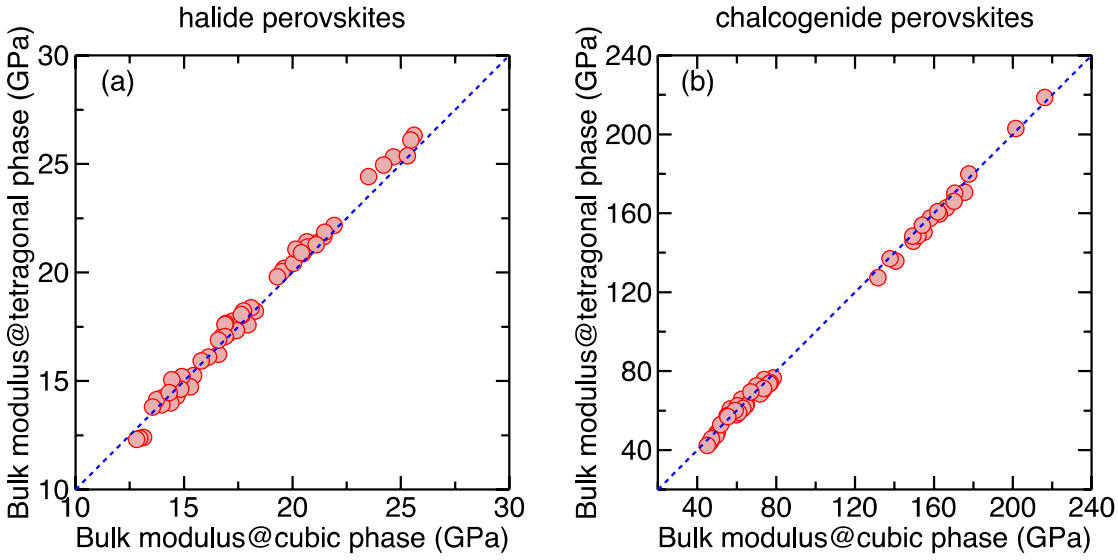

Figure S2. Bulk moduli (tetragonal phase vs cubic phase) of halide (a) and chalcogenide (b) perovskites. The data are taken from **Table S1**. The dashed diagonal line represents the ideal accord between the bulk moduli for the tetragonal and cubic phases.

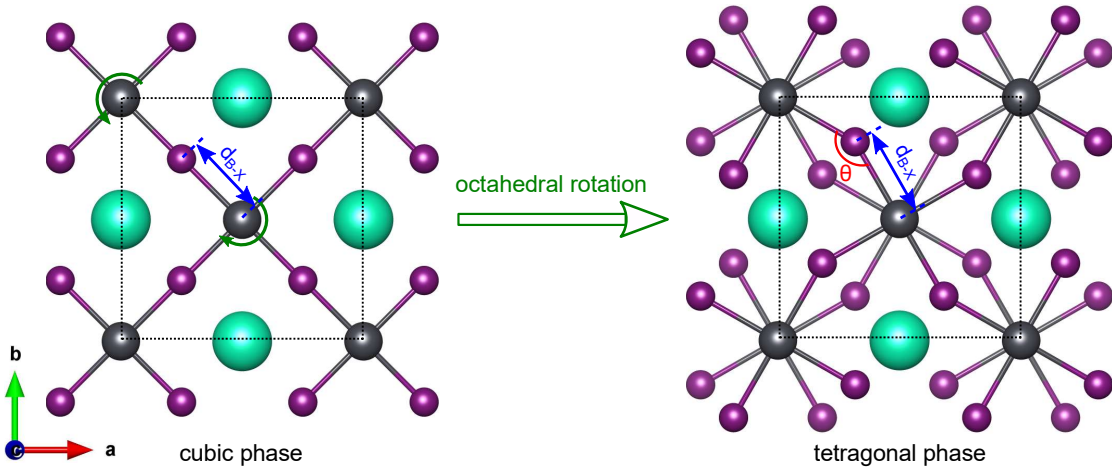

Figure S3. Structural illustration of perovskites transforming from the cubic phase to the tetragonal phase through octahedral rotation. The green, dark gray, and purple balls represent the A, B and X ions.

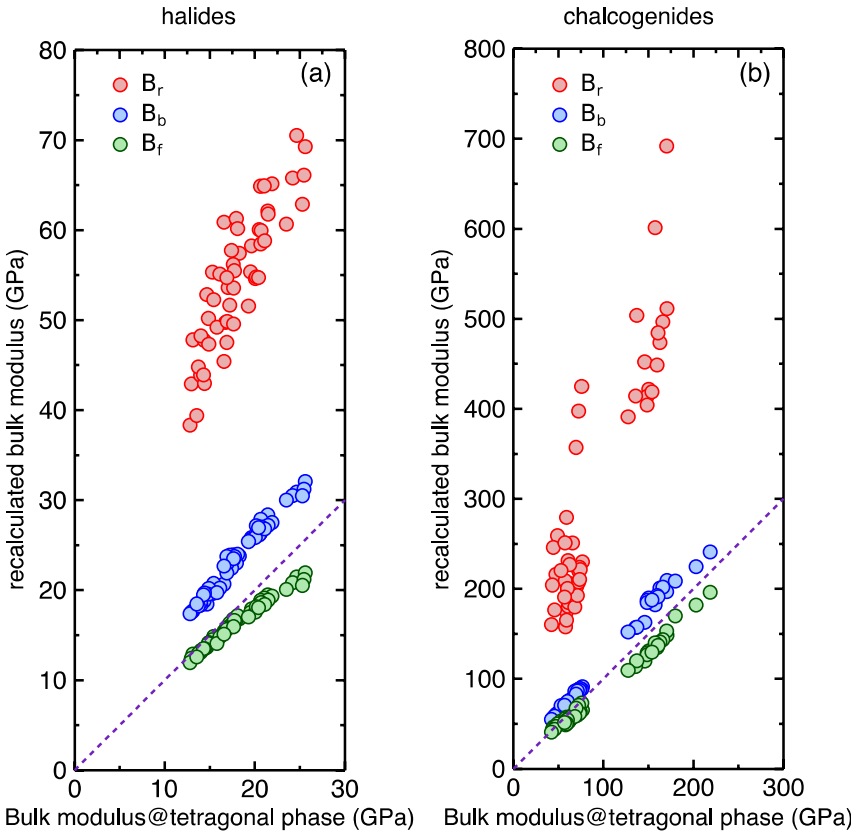

Figure S4. Recalculated bulk moduli (GPa) of perovskites by adopting tetragonal supercells resized through only rotating the BX_6 octahedra (B_r) or changing the length of B-X bonds in the ab plane (B_b) versus the normally calculated bulk moduli of perovskites in the tetragonal phase. B_f corresponds to the data obtained from the equation:$\frac{1}{B_f} = \frac{1}{B_r} + \frac{1}{B_b}$. The dashed violet lines represent the ideal accord between the recalculated and normal bulk moduli.

Table S2. Recalculated bulk moduli (GPa) of perovskites by adopting tetragonal supercells resized through only rotating the BX_6 octahedra (B_r) or changing the length of B-X bonds in the ab plane (B_b).

	$KCaCl_3$	$KCaBr_3$	$KCaI_3$	$KSrCl_3$	$KSrBr_3$	$KSrI_3$	$KBaCl_3$	$KBaBr_3$	$KBaI_3$
B_r	70.512	64.878	60.895	62.131	57.432	52.835	56.204	52.269	47.813
B_b	30.894	26.330	20.667	28.350	23.802	18.450	23.932	20.746	17.688
	$KGeCl_3$	$KGeBr_3$	$KGeI_3$	$KSnCl_3$	$KSnBr_3$	$KSnI_3$	$KPbCl_3$	$KPbBr_3$	$KPbI_3$
B_r	69.269	65.148	61.281	64.911	60.181	55.331	58.265	53.613	47.752
B_b	32.081	27.507	23.003	27.121	23.984	19.610	25.828	22.865	18.815
	$RbCaCl_3$	$RbCaBr_3$	$RbCaI_3$	$RbSrCl_3$	$RbSrBr_3$	$RbSrI_3$	$RbBaCl_3$	$RbBaBr_3$	$RbBaI_3$
B_r	65.779	60.049	55.109	58.450	53.572	48.261	51.650	47.343	42.898
B_b	30.499	26.131	20.245	27.878	23.454	18.358	23.887	20.203	17.546
	$RbGeCl_3$	$RbGeBr_3$	$RbGeI_3$	$RbSnCl_3$	$RbSnBr_3$	$RbSnI_3$	$RbPbCl_3$	$RbPbBr_3$	$RbPbI_3$
B_r	66.104	61.785	57.733	59.936	55.492	50.195	55.365	49.743	43.868
B_b	31.210	27.203	22.451	27.017	23.750	19.557	25.653	22.761	18.639
	$CsCaCl_3$	$CsCaBr_3$	$CsCaI_3$	$CsSrCl_3$	$CsSrBr_3$	$CsSrI_3$	$CsBaCl_3$	$CsBaBr_3$	$CsBaI_3$
B_r	60.665	54.615	49.201	54.799	49.847	44.794	47.522	42.972	38.336
B_b	30.016	25.861	19.716	27.166	22.976	18.240	23.737	19.679	17.381
	$CsGeCl_3$	$CsGeBr_3$	$CsGeI_3$	$CsSnCl_3$	$CsSnBr_3$	$CsSnI_3$	$CsPbCl_3$	$CsPbBr_3$	$CsPbI_3$
B_r	62.879	58.810	54.719	54.743	49.574	43.913	51.560	45.413	39.414
B_b	30.485	26.814	21.911	26.943	23.504	19.489	25.409	22.674	18.458
	$CaTiO_3$	$CaTiS_3$	$CaTiSe_3$	$CaZrO_3$	$CaZrS_3$	$CaZrSe_3$	$CaHfO_3$	$CaHfS_3$	$CaHfSe_3$
B_r	511.334	230.051	205.514	421.720	220.070	196.775	473.628	223.909	200.711
B_b	209.154	91.325	75.543	189.790	87.973	71.787	200.863	89.027	73.012
	$CaSiO_3$	$CaSiS_3$	$CaSiSe_3$	$CaGeO_3$	$CaGeS_3$	$CaGeSe_3$	$CaSnO_3$	$CaSnS_3$	$CaSnSe_3$
B_r	1048.694	424.839	279.305	691.800	250.988	258.979	452.022	231.362	246.043
B_b	240.998	88.472	72.237	196.850	78.092	61.741	162.844	72.485	56.971
	$SrTiO_3$	$SrTiS_3$	$SrTiSe_3$	$SrZrO_3$	$SrZrS_3$	$SrZrSe_3$	$SrHfO_3$	$SrHfS_3$	$SrHfSe_3$
B_r	496.610	221.412	195.184	413.902	202.363	174.728	448.523	207.518	180.477
B_b	201.840	89.136	74.497	187.309	87.162	71.430	192.462	87.798	72.353
	$SrSiO_3$	$SrSiS_3$	$SrSiSe_3$	$SrGeO_3$	$SrGeS_3$	$SrGeSe_3$	$SrSnO_3$	$SrSnS_3$	$SrSnSe_3$
B_r	958.481	397.483	251.059	601.107	226.874	215.970	414.324	208.979	204.204
B_b	224.603	85.859	71.245	182.338	76.086	60.260	156.883	71.437	55.724
	$BaTiO_3$	$BaTiS_3$	$BaTiSe_3$	$BaZrO_3$	$BaZrS_3$	$BaZrSe_3$	$BaHfO_3$	$BaHfS_3$	$BaHfSe_3$
B_r	484.412	210.505	184.914	404.060	179.802	157.721	418.861	192.483	165.193
B_b	191.233	87.394	73.350	184.567	86.205	70.804	187.663	86.668	71.806
	$BaSiO_3$	$BaSiS_3$	$BaSiSe_3$	$BaGeO_3$	$BaGeS_3$	$BaGeSe_3$	$BaSnO_3$	$BaSnS_3$	$BaSnSe_3$
B_r	915.761	357.070	220.256	503.594	200.480	176.416	391.112	190.921	160.312
B_b	208.576	82.863	70.208	157.303	74.745	58.622	152.147	70.515	54.831

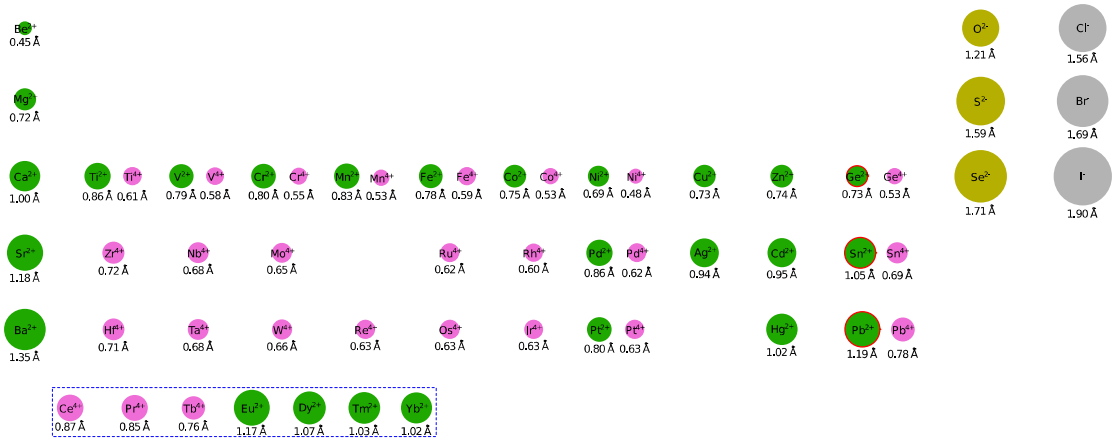

Table S3. The Shannon ionic radii of possible bivalent (green circles) and tetravalent (pink circles) metal cations in the periodic table with the coordination number of 6, and halide (yellow circles) and chalcogenide (gray circles) ions with the coordination number of 2. All data is extracted from the website: http://abulafia.mt.ic.ac.uk/shannon/radius.php, except the radii of Sn^{2+}, halide and chalcogenide ions, which are taken from [JACS, 2017, 139, 14905-14908]. The artificial or radioactive metal elements have been completely excluded. The cations with the lone pair *s* electrons are highlighted by the circles with the red edges. The lanthanide ions are remarked by the blue dashed rectangle.

Table S4. The sum ($r_B + r_X$) of the radii of considered bivalent metal ions (B^{2+}) and halide ions (X^-) and the predictive bulk modulus (B_P) following the equation $B_P = k \cdot (r_B + r_X)$, where k is the linear fitting coefficient extracted from the data for halide perovskites shown in Figure 2 of the main text.

	Cl^-		Br^-		I^-	
	$r_B + r_X$ (Å)	B_P (GPa)	$r_B + r_X$ (Å)	B_P (GPa)	$r_B + r_X$ (Å)	B_P (GPa)
Be^{2+}	2.01	84.72	2.14	65.93	2.35	45.34
Ni^{2+}	2.25	53.96	2.38	43.10	2.59	30.73
Mg^{2+}	2.28	51.17	2.41	40.99	2.62	29.35
Cu^{2+}	2.29	50.28	2.42	40.32	2.63	28.90
Ge^{2+}	2.29	50.28	2.42	40.32	2.63	28.90
Zn^{2+}	2.30	49.41	2.43	39.66	2.64	28.47
Co^{2+}	2.31	48.99	2.44	39.33	2.65	28.25
Fe^{2+}	2.34	46.12	2.47	37.15	2.68	26.81
V^{2+}	2.35	45.34	2.48	36.56	2.69	26.41
Cr^{2+}	2.36	44.58	2.49	35.97	2.70	26.02
Pt^{2+}	2.36	44.58	2.49	35.97	2.70	26.02
Mn^{2+}	2.39	42.38	2.52	34.29	2.73	24.90
Ti^{2+}	2.42	40.32	2.55	32.70	2.76	23.83
Pd^{2+}	2.42	40.32	2.55	32.70	2.76	23.83
Ag^{2+}	2.50	35.40	2.63	28.90	2.84	21.26
Cd^{2+}	2.51	34.84	2.64	28.47	2.85	20.96
Ca^{2+}	2.56	32.20	2.69	26.41	2.90	19.55
Hg^{2+}	2.58	31.21	2.71	25.64	2.92	19.02
Yb^{2+}	2.58	31.21	2.71	25.64	2.92	19.02
Tm^{2+}	2.59	30.73	2.72	25.26	2.93	18.76
Sn^{2+}	2.61	29.80	2.74	24.53	2.95	18.26
Dy^{2+}	2.63	28.90	2.76	23.83	2.97	17.77
Eu^{2+}	2.73	24.90	2.86	20.67	3.07	15.57
Sr^{2+}	2.74	24.53	2.87	20.38	3.08	15.37
Pb^{2+}	2.75	24.18	2.88	20.10	3.09	15.17
Ba^{2+}	2.91	19.28	3.04	16.19	3.25	12.40

Table S5. The sum ($r_B + r_X$) of the radii of considered tetravalent metal ions (B^{4+}) and chalcogenide ions (X^{2-}) and the predictive bulk modulus (B_P) following the equation $B_P = k\cdot(r_B + r_X)$, where k is the linear fitting coefficient extracted from the data for chalcogenide perovskites shown in Figure 2 of the main text.

	O^{2-}		S^{2-}		Se^{2-}	
	$r_B + r_X$ (Å)	B_P (GPa)	$r_B + r_X$ (Å)	B_P (GPa)	$r_B + r_X$ (Å)	B_P (GPa)
Ni^{4+}	1.69	302.14	2.07	134.24	2.19	107.15
Co^{4+}	1.74	268.88	2.12	122.02	2.24	97.90
Ge^{4+}	1.74	268.88	2.12	122.02	2.24	97.90
Mn^{4+}	1.74	268.88	2.12	122.02	2.24	97.90
Cr^{4+}	1.76	256.86	2.14	117.52	2.26	94.48
V^{4+}	1.79	240.07	2.17	111.15	2.29	89.62
Fe^{4+}	1.79	237.41	2.17	110.14	2.29	88.85
Rh^{4+}	1.81	229.64	2.19	107.15	2.31	86.56
Ti^{4+}	1.81	227.12	2.20	106.18	2.31	85.82
Pd^{4+}	1.82	222.18	2.21	104.26	2.33	84.35
Ru^{4+}	1.83	219.76	2.21	103.32	2.33	83.63
Ir^{4+}	1.83	217.38	2.21	102.39	2.33	82.91
Pt^{4+}	1.83	217.38	2.21	102.39	2.33	82.91
Os^{4+}	1.84	215.02	2.22	101.47	2.34	82.21
Re^{4+}	1.84	215.02	2.22	101.47	2.34	82.21
Mo^{4+}	1.86	205.92	2.24	97.90	2.36	79.46
W^{4+}	1.87	201.55	2.25	96.17	2.37	78.12
Nb^{4+}	1.89	193.16	2.27	92.82	2.39	75.54
Ta^{4+}	1.89	193.16	2.27	92.82	2.39	75.54
Sn^{4+}	1.90	189.12	2.28	91.21	2.40	74.29
Hf^{4+}	1.92	181.36	2.30	88.08	2.42	71.86
Zr^{4+}	1.93	177.64	2.31	86.56	2.43	70.69
Tb^{4+}	1.97	163.64	2.35	80.82	2.47	66.22
Pb^{4+}	1.98	158.75	2.37	78.79	2.48	64.64
Pr^{4+}	2.06	136.86	2.44	69.54	2.56	57.39
Ce^{4+}	2.08	131.68	2.46	67.30	2.58	55.63

Influence of isolated Pb 6s states on electronic properties of $MAPbI_3$

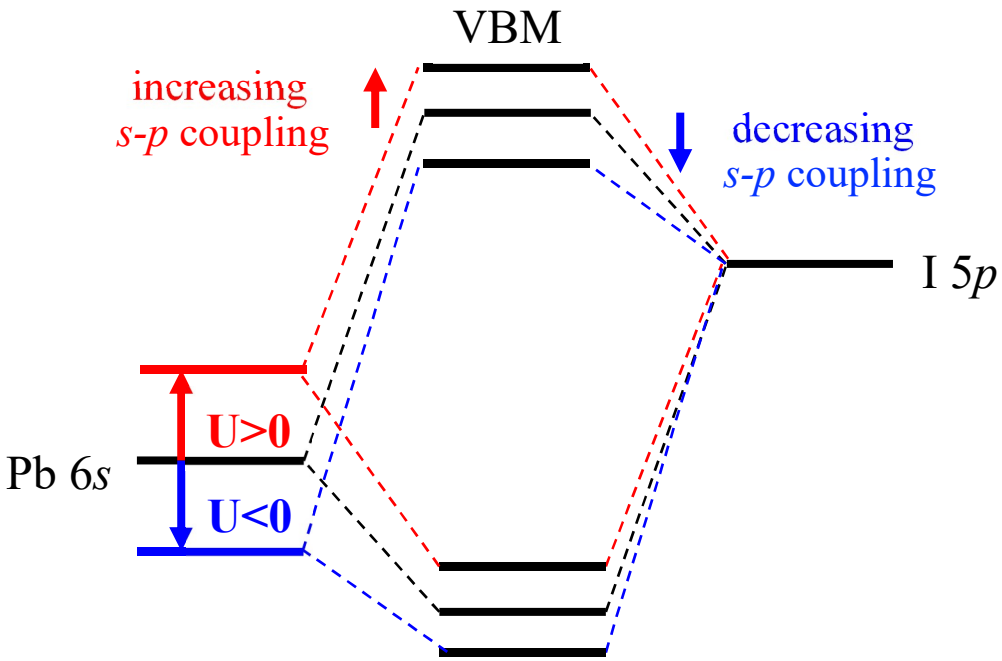

Figure S5. Schematic illustration of the modulation of energy levels and *s-p* antibonding coupling in LHPs under the application of a non-local external potential (U) on Pb 6*s* states.

We first discuss the influence of the isolated Pb 6s states on the band structures of $MAPbI_3$. It is experimentally found that $MAPbI_3$ possesses several different crystal structures and structural phases, which are dependent on the ambient temperature.[1] For the sake of simplicity, we take the cubic phase as an example. The calculated band structures under various nonlocal external potentials (U) are shown in Figure S6(a). The case of U= 0 eV corresponds to the regular PBE calculation. In this case, both the VBM and CBM are located at the R point, with an direct gap of 1.49 eV, which are in good agreement with results presented in previous work.[2] When the Pb 6s energy level is shift downward by applying a negative external potential (U= -3 eV), the CBM goes up slightly, while the VBM changes significantly, with a fall of 0.64 eV, thus leading to a much bigger bandgap of 2.23 eV (cf. Figure S6(b)). These changes can be attributed to the decreased antibonding coupling between the I 5p states and the Pb 6s states, due to their enlarged energy difference (cf. Figure S5). The weaker coupling consequently brings down the I 5p states, which are the main component of VBM. Reversely, when a positive potential (U= +3 eV) is adopted to raise the Pb 6s energy level, we notice the opposite influence exerted on the band structures: a small drop of CBM and a dramatic rise of VBM being up to 0.72 eV, which together result in a remarkably reduced band gap (0.66 eV) (cf. Figure S6(a) and (b)). Similarly, all the changes induced by the application of U = +3 eV, can be explained by the increased *s-p* antibonding coupling, as a result of their shrunken energy difference (cf. Figure S5). Last but not the least, the application of an external potential (U) on the Pb 6s states does not alter the direct gap

character of $MAPbI_3$, namely both VBM and CBM being always located at the R point. What's more, Yin's work[2] has pointed out the *s-p* antibonding coupling make upper valence bands dispersive, and hence results in a small hole effective mass, which can also be seen from Figure S6(a). More importantly, we notice that the upper valence band dispersion is dramatically modified upon various U. This observation is the direct consequence of the change of the *s-p* antibonding coupling: the more positive U, the stronger coupling, the more dispersion, and the lighter hole effective mass. This relationship is clearly illustrated in Figure S6(b), where we notice the average hole effective mass (m_h^*) linearly decreases as U increases. When U = +3 eV, m_h^* reduces to $0.088\ m_e$, being almost half of that ($0.168\ m_e$) for U = 0 eV. The hole effective mass along the directions of $R \rightarrow X$, $R \rightarrow M$ and $R \rightarrow \Gamma$ is also calculated. They differ slightly from each other upon the same U and all undergo a linear decrease when U increases, as shown in Figure S6(c). Through this study, we provide firm evidences to verify that applying the nonlocal external potential U on Pb 6s states can efficiently tune the *s-p* antibonding coupling, which in turn modifies the electronic structure and hole effective mass of $MAPbI_3$.

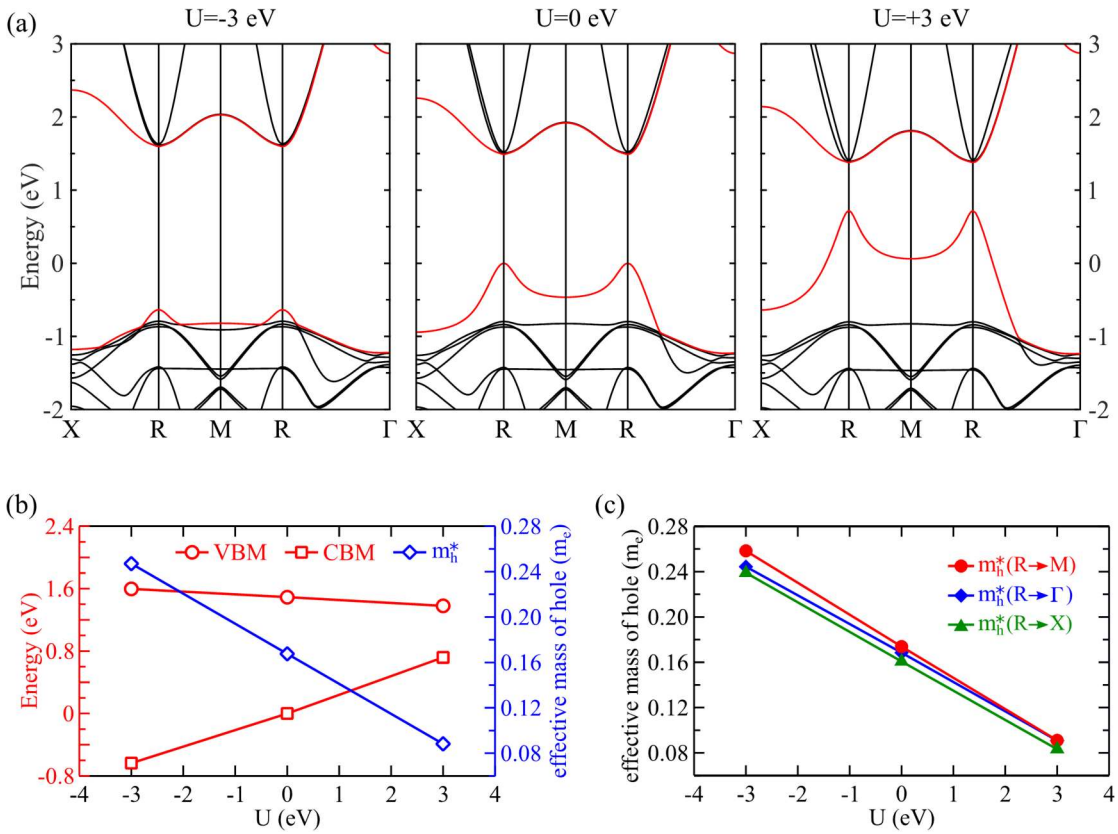

Figure S6. (a) Band structures of $MAPbI_3$ in the cubic phase calculated under various external potentials (U). The bands referring to VBM and CBM are highlighted in red. All the bands are plotted with respect to the VBM obtained upon U = 0 eV, which is shift to 0. (b) Positions of band edges (red) and average hole effective mass (blue) as a function of U. (c) Calculated hole effective mass along the directions of $R \rightarrow M$, $R \rightarrow \Gamma$ and $R \rightarrow X$.

The change of the *s-p* antibonding coupling as a function of U can also be seen from the partial charge densities at VBM, as shown in Figure S7(a). Obviously, the VBM consists of Pb 6s orbitals and I 5p orbitals. In addition, an evident antibonding character for Pb-I bonds is noticed that: densities of electrons are well concentrated around Pb and I atoms, leaving extremely low density at the center of the bond. In order to facilitate comparison, the charge density differences between calculations with U = -3 and 0 eV, and that between calculations with U = +3 and 0 eV are shown in Figure S7(b). Upon U = -3 eV, the partial charge density decreases around Pb atoms and increases around I atoms compared to that obtained upon U = 0 eV. Oppositely, the partial charge density increases around Pb atoms and decreases around I atoms when U = +3 eV. This implies the increased contribution of Pb 6p states to VBM as U increases, which is revealed in Figure S7(c). In order to clearly demonstrate the change of the *s-p* antibonding coupling under various U, the localization of partial charge densities at VBM is quantified by computing the inverse participation ratio (IPR).[3] The definition of IPR for a particular Kohn-Sham orbital is given by the following equation:

$$\mathrm{IPR} = N \cdot \frac{\sum_{i=1}^{N} {\rho_i}^2}{(\sum_{i=1}^{N} \rho_i)^2}$$

$$\mathrm{IPR} \in [1, N],$$

where N represents the number of grids of a given Kohn-Sham state and ρ_i denotes the charge density at the grid i. From this formula, we note that larger and smaller IPR correspond to more localized and delocalized states, respectively. Ideally, $\mathrm{IPR} = N$ means a totally localized state. As shown in Figure S7(c), the IPR becomes larger when U increases, agreeing with our preceding conclusion that more positive U leads to the more localized charge density and the stronger *s-p* antibonding coupling. What's more, we notice that the IPR and percentage of Pb 6s orbital contribution to VBM are no longer linearly dependent on U, and both show bigger changes upon U = +3 eV than that upon U= -3 eV, as compared to the reference achieved with U = 0 eV, which implies that the change of the *s-p* antibonding coupling is more sensitive to the reduction of the energy difference between Pb 6s and I 5p levels than the enlargement of the counterpart.

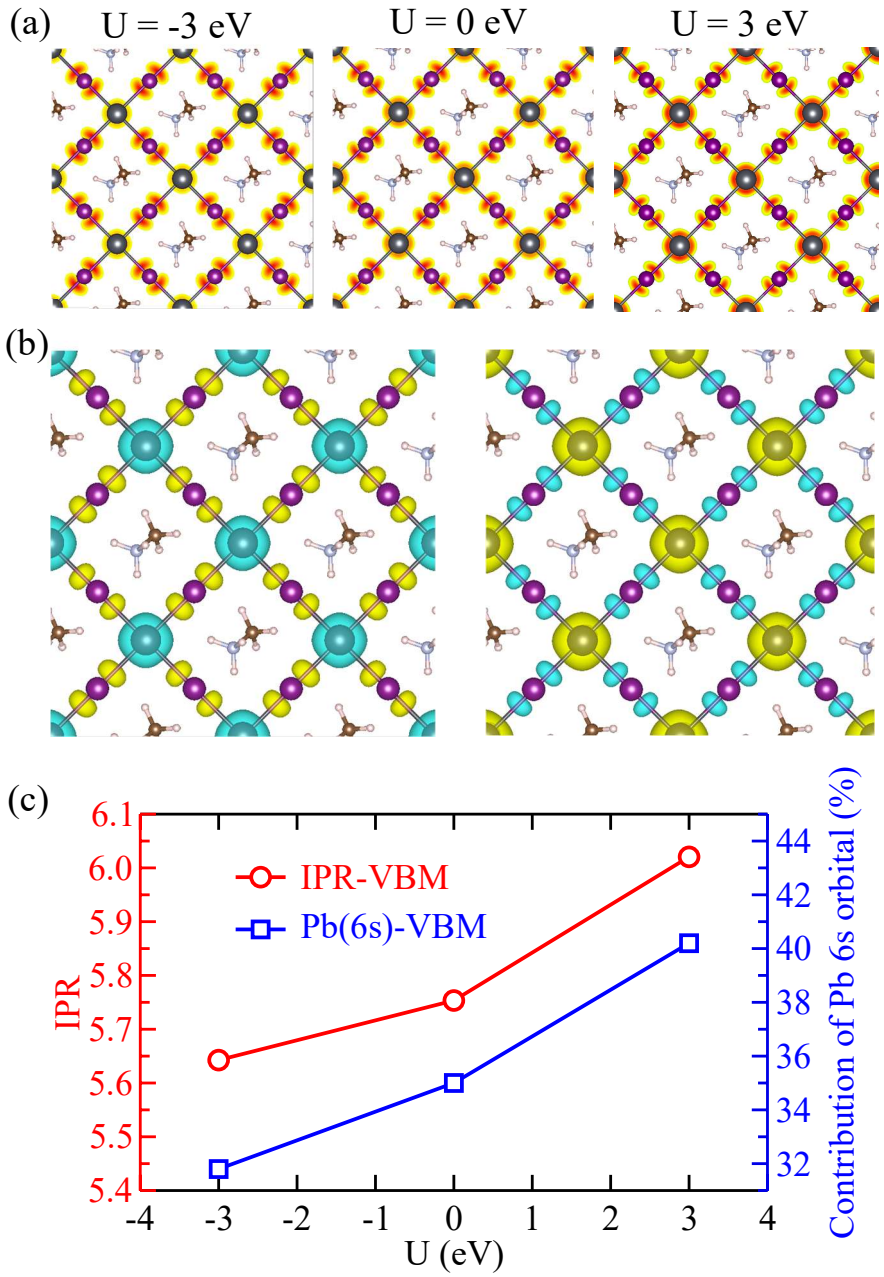

Figure S7. (a) Partial charge densities at VBM for U = -3 eV (left), 0 eV (middle) and +3 eV (right). The darker the red color, the higher the electron density. (b) Charge density differences between calculations under U = -3 and 0 eV (left), and that between calculations under U= +3 and 0 eV (right). The cyan and yellow colors indicate the charge density decreasing and increasing, respectively. (c) Inverse participation ratio (IPR) of partial charge densities (red, left) and the percentage of Pb 6s orbital contribution to VBM (blue, right) versus U. In this figure, the gray and purple balls represent Pb and I atoms, respectively.

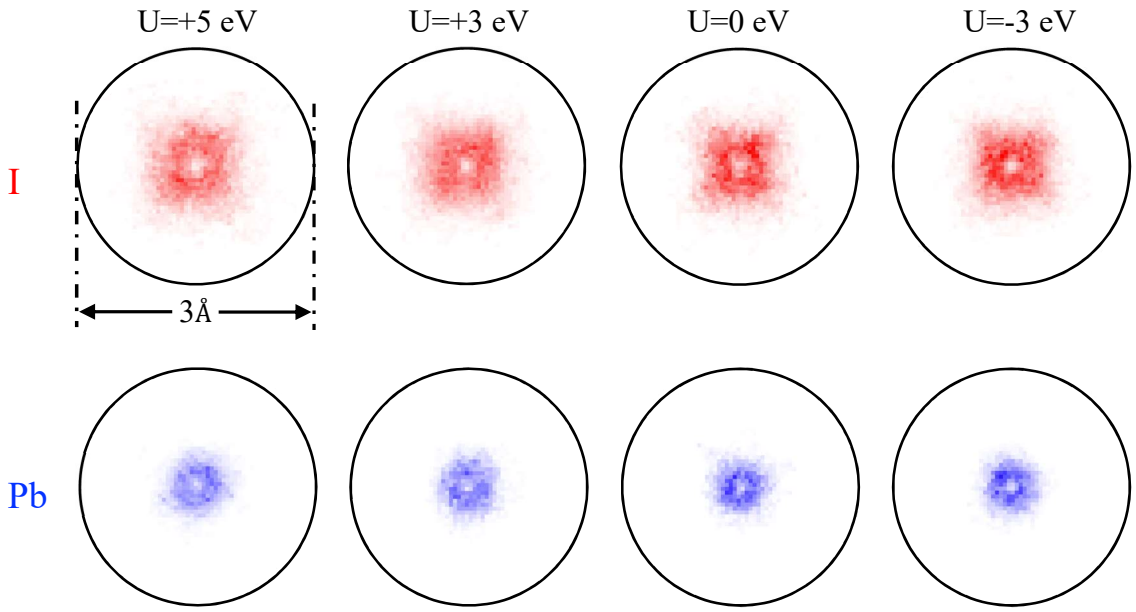

Figure S8. Distribution of moving I (red) and Pb (blue) atoms in 5ps MD trajectories of β-$MAPbI_3$ projected in the X-Y plane. The darker color, the higher intensity. The center of the circle corresponds to the average position of each atom during the MD run and the diameter of the circle is 3Å.

Table S6. The overlap integral (I_{OV}), the average root-mean-square (RMS) velocity (υ) of component atoms, the absolute value of NA electron-phonon coupling (|NAC|) and the nonradiative carrier lifetime (τ_{nr}) for GaAs and β-$MAPbI_3$ achieved at various temperature.

	GaAs					β-$MAPbI_3$				
	I_{OV}	ν_{Ga}(Å/fs)	ν_{As}(Å/fs)	|NAC| (meV)	τ_{nr}(ns)	I_{OV}	ν_{Pb}(Å/fs)	ν_{I}(Å/fs)	|NAC| (meV)	τ_{nr}(ns)
100 K	0.6641	0.00188	0.00182	0.0839	105.24	0.5754	0.00108	0.00139	0.242	34.18
200 K	0.6607	0.00266	0.00258	0.2124	23.43	0.5517	0.00152	0.00199	0.201	60.43
300 K	0.6573	0.00326	0.00316	0.3884	5.56	0.5029	0.00187	0.00242	0.149	91.36
400 K	0.6535	0.00379	0.00363	0.5250	3.24	0.4386	0.00220	0.00277	0.101	125.57

Reference:

1. P. S. Whitfield, N. Herron, W. E. Guise, K. Page, Y. Q. Cheng, I. Milas and M. K. Crawford, *Sci. Rep.*, 2016, **6**, 35685.
2. W.-J. Yin, T. Shi and Y. Yan, *Appl. Phys. Lett.*, 2014, **104**, 063903.
3. Y. Wang and R. Long, *ACS Appl. Mater. Interfaces*, 2019, **11**, 32069-32075.